Capacitive Micromachined Ultrasonic Lamb Wave Transducers Using Rectangular Membranes

Mohammed H. Badi, *Student Member, IEEE*, Goksen G. Yaralioglu, *Member, IEEE*, A. Sanli Ergun, *Member, IEEE*, Sean T. Hansen, *Student Member, IEEE*, Eehern J. Wong, and Butrus T. Khuri-Yakub, *Fellow, IEEE*

***Abstract*—This paper details the theory, fabrication, and characterization of a new Lamb wave device. Built using capacitive micromachined ultrasonic transducers (CMUTs), the structure described uses rectangular membranes to excite and receive Lamb waves on a silicon substrate. An equivalent circuit model for the transducer is proposed that produces results, which match well with those observed by experiment. During the derivation of this model, emphasis is placed on the resistance presented to the transducer membranes by the Lamb wave modes. Finite element analysis performed in this effort shows that the dominant propagating mode in the device is the lowest order antisymmetric flexural wave (A_0). Furthermore, most of the power that couples into the Lamb wave is due to energy in the vibrating membrane that is transferred to the substrate through the supporting posts of the device. The manufacturing process of the structure, which relies solely on fundamental IC-fabrication techniques, is also discussed. The resulting device has an 18-μm-thick substrate that is almost entirely made up of crystalline silicon and operates at a frequency of 2.1 MHz. The characterization of this device includes S-parameter and laser vibrometer measurements as well as delay-line transmission data. The insertion loss, as determined by both S-parameter and delay-line transmission measurements, is 20 dB at 2.1 MHz. When configured as a delay-line oscillator, the device functions well as a sensor with sensitivity to changes in the mass loading of its substrate.**

I. Introduction

The first detailed description of Lamb waves was published by Sir Horace Lamb in 1917 [1]. The characteristics of these waves have since been explored by many authors [2], [3] and numerous acoustic wave devices have been built using the excitation of Lamb waves as their primary vehicle of transduction. Most of these devices [4]–[8] rely on an interdigital electrode configuration [9] at the surface of piezoelectric ceramics. Other methods of Lamb wave excitation rely on electrostrictive [10], thermoelastic [11], magnetic, magnetostrictive [12], and Hertzian contact [13] structures. These structures support practical applications in the fields of sensors [5], [10], [14], [15] and microtransport [16]. Most Lamb wave devices take advantage of the fact that the velocity of the lower-order modes is often smaller than the speed of sound in the surrounding media. This is desirable because, as explained by Huygen's Principle, it can result in a relatively low-loss acoustic waveguide.

This paper introduces a new method to excite and detect Lamb waves using the capacitive micromachined ultrasonic transducer (CMUT). The CMUT is similar to other air-coupled capacitance transducers [17], [18] and has traditionally been used to send and receive ultrasound in air and in water. Its invention was reported in 1994 [19], and it has since found applications in nondestructive evaluation [21], ultrasound imaging [22], microfluidics [23], [24], and acoustic sensing using optical and radio frequency detection [25], [26]. The excitation of Lamb wave modes in CMUTs was first discovered during the characterization of 1-D CMUT arrays for medical imaging [27], in which a dip was noted in the radiation pattern of a single-array element, indicating a spurious radiating mode in the structure. The angle of this dip varied with frequency suggesting that energy was coupling into a wave mode with dispersive characteristics. Further analysis concluded that this mode belonged to a Lamb wave. The presence of Lamb waves in devices built for the purpose of transmitting an acoustic signal into the surrounding medium (e.g., air, water, oil) has a deleterious effect on the system behavior [28], [29]. This is because the wave that is excited presents an energy loss mechanism to the membrane and creates a cross-coupling of energy between otherwise independent cells. If this excitation of Lamb waves is instead exploited and optimized, however, the foundation for a new device is created. A proof of principle of this idea, along with a preliminary theoretical analysis of the concept, can be found in [30]–[32]. This paper reports advances in the work done on capacitive micromachined ultrasonic Lamb wave transducers, including a detailed analysis of their equivalent circuit model as well as a thorough characterization of fabricated devices using a variety of measurement tools. It should also be noted that the devices described in this paper have significantly superior characteristics than those that have been discussed in previous publications on this topic.

The devices described in this paper use high aspect ratio rectangular membranes. As most CMUTs are made from nearly circular membranes, this change in shape necessitates a different formulation of the equivalent circuit model

Manuscript received August 28, 2002; accepted May 21, 2003. This work was supported by the United States Office of Naval Research under Grant N00014-94-1-073.

All authors are with the E. L. Ginzton Laboratory, Stanford, CA 94305-4088 (e-mail: mbadi@echo.stanford.edu).

parameters used to describe the behavior of the transducers. Thus, after a theoretical discussion of Lamb waves and Lamb wave excitation using CMUTs, this paper presents equations that govern rectangular membranes and their implications in the equivalent circuit model. The highlight of this section is a formulation of the resistance presented to these membranes by the Lamb wave modes in the silicon plate. A summary of the manufacturing process of the devices is then presented, followed by a detailed section on the device characterization. The characterization includes S-parameter and laser vibrometer measurements, delay-line transmission data, and preliminary results from a humidity sensor. The paper concludes with a description of plans for future work.

II. Theoretical Formulation

A. Lamb Waves

Lamb and Love waves describe two types of normal modes, also called plate modes, that can exist in a plate with free boundaries. In a Lamb wave the displacement of the particles occurs both in the direction of wave propagation and perpendicular to the plane of the plate. This wave has two groups of modes that can independently satisfy the wave equation: symmetric and antisymmetric [2]. The symmetric modes are also referred to as longitudinal modes because the average displacement over the plate thickness is in the longitudinal direction. The motion of antisymmetric modes is in the transverse direction, and as a result they are also known as flexural modes [33].

The dispersion relation that governs Lamb waves in homogenous, isotropic plates is presented in [2], [3], [33], and the equations for the symmetric and antisymmetric modes are given in (1) and (2), respectively.

$$\frac{\tan k_{ts}b/2}{\tan k_{tl}b/2} = -\frac{4\beta^2 k_{tl}k_{ts}}{\left(k_{ts}^2-\beta^2\right)^2} \tag{1}$$

$$\frac{\tan k_{ts}b/2}{\tan k_{tl}b/2} = -\frac{\left(k_{ts}^2-\beta^2\right)^2}{4\beta^2 k_{tl}k_{ts}} \tag{2}$$

$$k_{tl}^2 = \left(\frac{\omega}{V_l}\right)^2 - \beta^2 \quad k_{ts}^2 = \left(\frac{\omega}{V_s}\right)^2 - \beta^2.$$

In these transcendental equations, also known as the Rayleigh-Lamb frequency equations, ω is the angular frequency, β is the wave number, b is the plate thickness, and V_l and V_s are the longitudinal and shear velocities, respectively. The curves for the zero-order antisymmetric and symmetric dispersion relation are plotted in Fig. 1. The longitudinal and shear velocities were calculated under the assumption that silicon acts like an isotropic material. This figure indicates several important characteristics of the dispersion curves. First, the velocity of the A_0 mode drops to zero for vanishing plate thicknesses, while that of the S_0 mode levels out at a much higher velocity. Second, as the thickness of the plate upon which the wave is traveling becomes much larger than the wavelength, both modes asymptotically approach the Rayleigh velocity. Finally, below a certain frequency-thickness product, the A_0 and S_0 modes are the only ones that can exist on the plate; all other modes are cut off.

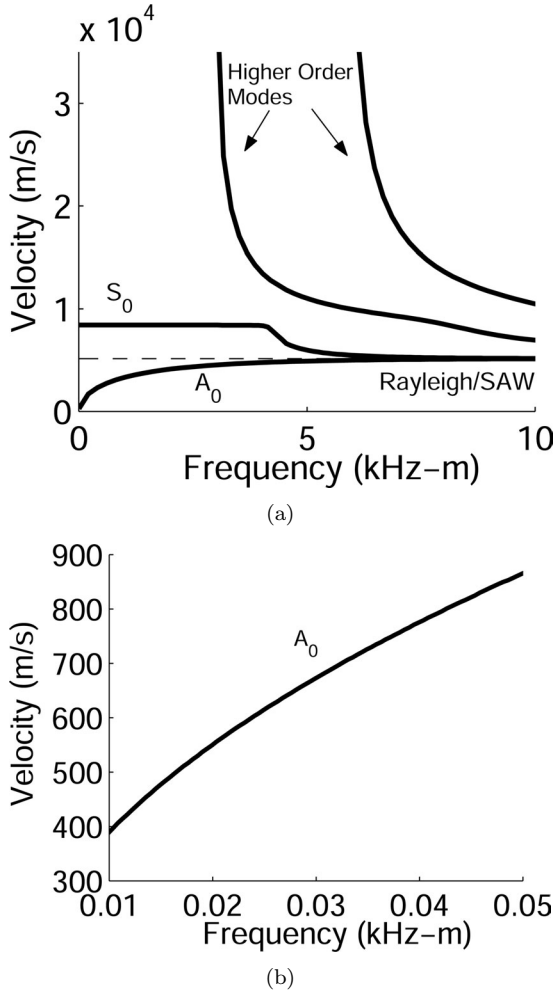

Fig. 1. (a) Select Lamb and Rayleigh velocities on silicon. (b) An expansion of the A_0 curve for frequency-thickness values near 0.038 kHz-m, the operating point of the devices discussed in this paper. The calculations used to create both plots treat silicon as an isotropic material. The constants are taken from [34] V_s = 5840.9 m/s, V_l = 8429.4 m/s.

The devices described in this paper operate in the 2.1-MHz range with a plate thickness of 18 μm. At this frequency-thickness product the A_0 and S_0 modes are the only ones that are excited, and their velocities under the isotropic assumption are 737 m/s and 8423 m/s, respectively. When compared with the speed of a Lamb Wave along the $\langle 110 \rangle$ direction as predicted by the surface impedance method [35], these values are correct to within 2%.

B. Lamb Waves Using CMUTs

The devices described in this paper use rectangular CMUTs. As shown in Fig. 2, the membranes are 77 μm

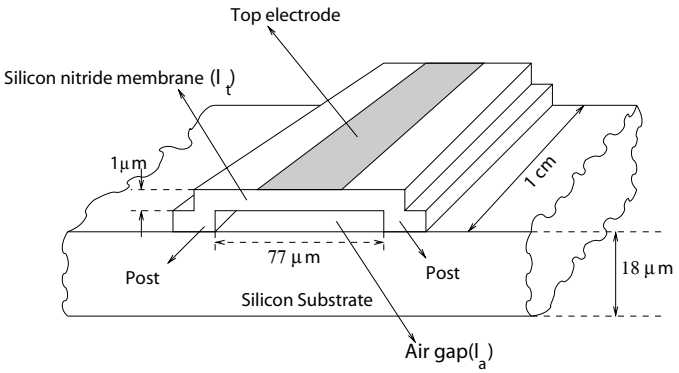

Fig. 2. Diagram of a single CMUT membrane.

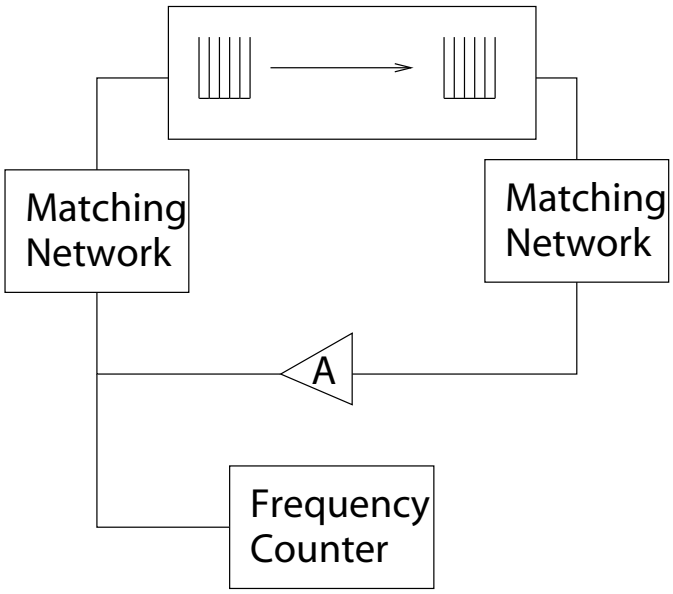

Fig. 3. Experimental setup of the delay-line oscillator.

wide, 1 cm long, and 1 μm thick with a gap of 1 μm. An aluminum electrode covers half of the surface of the membrane and acts as one of the capacitor's electrodes. The other electrode, not shown on the figure, is a thin highly doped region on the top of the silicon surface. The dominant time varying force on the membrane of a CMUT is proportional to the product of the dc and ac potentials applied to these electrodes [20]. As a result, the signal sent to the CMUT has the two voltages superimposed on each other. With this setup, the membrane will vibrate with a resonant characteristic determined by the geometry of the structure [see (5)]. As explained in the next section, energy from this vibration then couples through the posts shown in Fig. 2 to excite Lamb waves in the silicon plate. While both of the zero-order modes are excited in the substrate, the dominant mode that propagates is the lowest-order antisymmetric flexural wave (A_0). In order to reinforce the acoustic energy created by a single CMUT, fifteen transmitting membranes are spaced with a period of one wavelength on the same substrate to foster constructive interference. Due to the large aspect ratio of the membranes, the wave propagation can be approximated as a plane wave away from the membrane in the lateral direction. The Lamb waves are sensed further down the substrate by an identical set of fifteen receiving membranes. In the case of the devices presented here, the distance between the transmitting and receiving membranes is approximately 7.8 mm.

One commonly used figure of merit for a Lamb wave device is its insertion loss. The minimum value that can be obtained for a device such as this is 6 dB. This value assumes perfect electromechanical coupling both into and out of the A_0 mode of the Lamb Wave. The losses that do exist are the result of a splitting of the wave into two directions at both the transmitting and receiving membranes. This insertion loss can be measured from the S-parameters of the system or from the amplifier setting when the device is wired as a delay-line oscillator. The diagram in Fig. 3 outlines the setup for the latter case; the amplifier is used to compensate for losses in the device, and as such its gain is equal to the device insertion loss. The frequency of oscillation is determined by (3), which is derived from the condition that the total phase shift around the loop be an integral number of wavelengths [36]. In this equation,

$$f = \frac{v_p}{2\pi L}\left(2\pi N - \phi_E\right) \tag{3}$$

v_p is the phase velocity of the mode being observed, L is the acoustic path length (defined as the distance between the centers of the transmitting and receiving membranes), N is an integer greater than zero, and ϕ_E is the electronic phase shift through the amplifier. For a device in which the geometry and amplifier phase shift are fixed, the oscillation condition is determined by the value of N that corresponds to the frequency with the lowest insertion loss.

It is clear from (3) that the oscillation frequency is a function of the phase velocity of the Lamb wave in the channel. This relationship provides the basis for using such devices as sensors. When the velocity is influenced by any number of measurands (such as mass loading of the substrate or a change in its elastic stiffness), a shift in the operating frequency will result. By measuring the value of this shift, characteristics of the influencing factor can be determined.

C. Rectangular Membranes

Most devices fabricated using CMUT technology have membranes that closely approximate circles. Theoretical models for these membranes are relatively well developed [37], [38], and they have been applied to equivalent circuits that match well with experimental results [39], [40]. The membranes in the devices described in this paper, however, are rectangular, and, as a result, a different set of equations is necessary to describe their behavior. The derivation and presentation of these equations, for the purpose of creating an equivalent circuit model of a Lamb wave device based

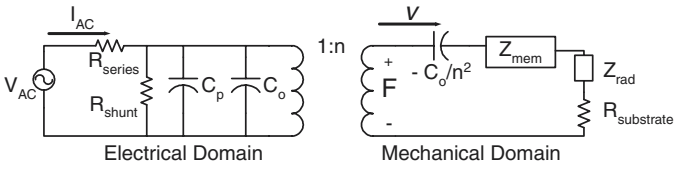

Fig. 4. Equivalent circuit model of a transmitting CMUT.

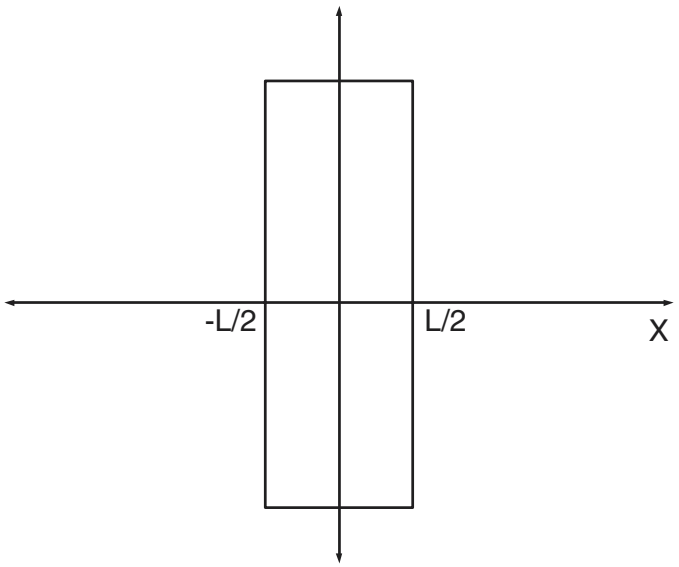

Fig. 5. Orientation of the rectangular membrane used to solve (4).

on CMUTs, is the subject of this section. The skeleton for this model is shown in Fig. 4 and is based on the standard equivalent circuit for an electromechanical transducer [42]. On the electrical side, the input for the circuit is an ac voltage source, V_{AC}, from which the source current, I_{AC}, is pulled. On the mechanical side of the circuit, the voltage is transformed from the electrical domain using the turns ratio, n, to a force labeled F. This force is defined to be uniform over the surface of the membrane. The velocity that results, v, is defined as the average velocity over the width of the membrane. All of the expressions that follow treat the case of a single rectangular membrane.

1. Membrane Impedance: Z_{mem}: The membrane impedance is defined as the ratio of an applied uniform force on a membrane to the average velocity over the membrane of the resulting motion. Texts that derive the expression for a rectangular membrane generally do so for either a thin-stretched membrane, wherein the bending stiffness is negligible or for thick geometries in which the tension is assumed to be insignificant. The membrane thickness of the devices presented in this paper are between these two extremes. The derivation that follows thus takes the effects of both bending stiffness and tension into account.

Consider a stretched membrane with Young's Modulus Y_0, Poisson's Ratio σ, under a tensile stress T, with an applied uniform net pressure over the membrane surface of P and a density of ρ. The differential equation governing the normal displacement $u_{AC}(x)$ of this membrane (derived from energy considerations) can be written as [37]:

$$\frac{(Y_0+T)l_t^3}{12(1-\sigma^2)}\nabla^4 u_{AC} - Tl_t\nabla^2 u_{AC} - P + l_t\rho\frac{d^2\omega}{dt^2} = 0. \tag{4}$$

Assuming that the aspect ratio of the membrane is large and using the steady state condition, the membrane response and thus (4) can be reduced to a one-dimensional problem in the x-direction. The clamped boundary condition (both the displacement and slope of the displacement of the membrane at the edges is zero) is used to solve this problem under the orientation shown in Fig. 5. The resulting solution for $u_{AC}(x)$, the displacement as a function of position, is

$$\begin{aligned}
u_{AC}(x) &= 2c_{12}\cosh(k_1x) + c_3\cos(k_3x) - \frac{P}{\rho l_t\omega^2}\\
c_{12} &= \frac{k_3P\sin\frac{k_3L}{2}}{l_t\rho\omega^2\left(2k_1\cos\frac{k_3L}{2}\sinh\frac{k_1L}{2} + 2k_3\sin\frac{k_3L}{2}\cosh\frac{k_1L}{2}\right)}\\
c3 &= \frac{\sinh\frac{k_1L}{2}k_1P}{l_t\rho\omega^2\left(k_1\cos\frac{k_3L}{2}\sinh\frac{k_1L}{2} + k_3\sin\frac{k_3L}{2}\cosh\frac{k_1L}{2}\right)}\\
k_1 &= \sqrt{\frac{d+\sqrt{d^2+4c\omega^2}}{2c}}\\
k_3 &= \sqrt{\frac{-d+\sqrt{d^2+4c\omega^2}}{2c}}\\
c &= \frac{(Y_0+T)\,l_t^2}{12\rho(1-\sigma^2)}\\
d &= \frac{T}{\rho}.
\end{aligned} \tag{5}$$

The next step in determining the membrane impedance is to find the average displacement over the short dimension of the membrane and to find its time harmonic derivative (the equivalent of multiplying by $j\omega$) to obtain the velocity v. Finally, using the initial assumption of a pressure P applied to the membrane, the impedance $Z_{\text{mem}} = \frac{P}{v}$ [mks-Rayls] can be written as

$$Z_{\text{mem}} = j\left(\frac{k_1k_3Ll_tP\rho\omega}{k_1k_3LP - 2c_3k_1l_t\rho\omega^2\sin\frac{k_3L}{2} - 4c_{12}k_3l_t\rho\omega^2\sinh\frac{k_1L}{2}}\right). \tag{6}$$

The constants k_1, k_3, c_{12}, and c_3 are defined in (5). Although it is not immediately obvious, (6) is independent of pressure as the P terms cancel out. They are left in the equations above in order to avoid redefining the previously listed constants. Note that the conventions set forth in Fig. 4 use force and velocity relationships in the mechanical domain. As a result, the expression in (6) should be multiplied by the device area before it is applied to the equivalent circuit.

2. Device Capacitance: C_0: The equivalent circuit of Fig. 4 is also dependent on the expression of C_0, the static (DC) capacitance of the CMUT. As shown in Fig. 2, a rectangular CMUT membrane consists of a metalized layer with an area A, a silicon nitride layer of thickness l_t, a vacuum gap of thickness $l_a(x)$. The latter term is actually a function of the lateral dimension, x, and thus can also be written as $(l_{a0} - u_{DC}(x))$ in which l_{a0} is the thickness of the gap without any membrane deflection, and u_{DC} is a measure of the static deflection. Also present on the device, but not shown in the figure, is a thin silicon nitride insulation layer directly above the substrate of thickness l_i. Neglecting fringing fields, the capacitance of this structure is given by

$$C_0 = \frac{\epsilon_0 \epsilon_r A}{l_t + l_i + \epsilon_r (l_{a0} - u_{DC}(x))} \tag{7}$$

where ϵ_0 is the dielectric constant in air and ϵ_r is the relative permittivity constant of silicon nitride.

An expression for $u_{DC}(x)$, the static deflection of the membrane, is thus necessary to accurately model the static device capacitance. While this can be done by taking the expression from (5) and finding its limit at very small frequencies, it is easier to find a qualitative expression by redoing the derivation starting with (4) and setting the frequency term to zero. After some mathematical steps similar to those used to derive the membrane impedance (see Appendix), the following expression for the membrane deflection is obtained:

$$\begin{aligned} u_{DC}(x) &= \frac{LP}{8d'k_3'}\left(k_3'L - 4\coth\frac{k_3'L}{2}\right) \\ &\quad + \frac{LP}{2d'k_3'}\frac{\cosh k_3'x}{\sinh\frac{k_3'L}{2}} - \frac{Px^2}{2d'} \\ k_3' &= \sqrt{\frac{d'}{c'}} \\ c' &= \frac{(Y_0+T)l_t^3}{12(1-\sigma^2)} \quad d' = Tl_t. \end{aligned} \tag{8}$$

A plot of the static displacement, $u(x)$, as a function of position for the lowest order mode is given in Fig. 6. The substitution of (8) into (7) yields C_0, the static capacitance of a single rectangular membrane.

3. Radiation Impedance: Z_{rad}: As a result of the motion of the rectangular membrane, the surrounding acoustic medium exerts a reaction force on it that is related to the velocity of the membrane through the radiation impedance. The derivation of this impedance treats the structure as a piston in a rigid infinite baffle. Approximate expressions for the impedance reported in [41] are repeated here and used in the model of Fig. 4. These expressions were obtained by relating the radiation impedance of a rectangular membrane to the Fourier transform of its impulse response.

$$Z_n(kb) = \rho c A_n [R_n(kb) + jX_n(kb)] \tag{9}$$

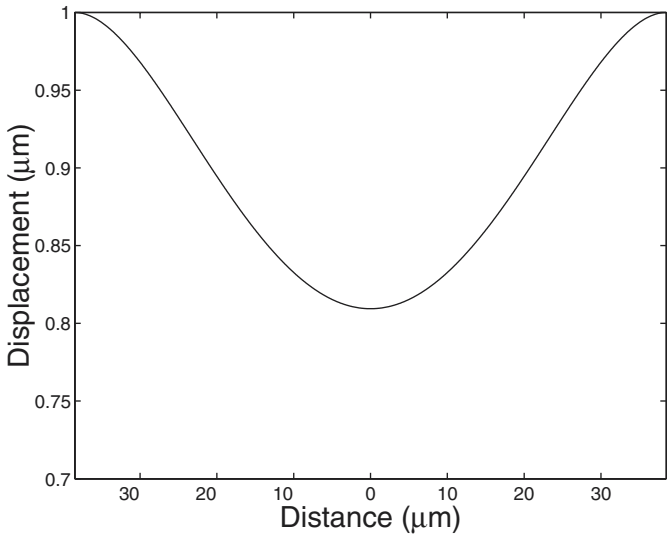

Fig. 6. Static membrane deflection as a function of location for a 77 μm wide membrane with a 1-μm gap. The ambient pressure on the membrane in this simulation is 101.3 kPa. The constants used in this simulation are $Y_0 = 3.2 \times 10^{11}$ Pa, $\sigma = 0.263$, $\rho = 2843$ kg/m^3, T = 100 MPa.

$$\begin{aligned} R_n(kb) &\sim 1 - \left(\frac{2}{\pi n (kb)^2}\right) \\ &\quad \left(1 - \cos kb - \cos nkb + \cos([n^2+1]^{\frac{1}{2}}kb)\right) \\ &\quad + \left(\frac{2}{\pi}(kb)^3\right)^{\frac{1}{2}} \cos\left(kb + \frac{3\pi}{4}\right) \\ &\quad + \left(\frac{2}{\pi}(nkb)^3\right)^{\frac{1}{2}} \cos\left(nkb + \frac{3\pi}{4}\right) \\ X_n(kb) &\sim \left(\frac{2(1+n)}{n\pi kb}\right) \\ &\quad - \left(\frac{2}{n\pi(kb)^2}\right)\left(\sin kb + \sin nkb - \sin kb\left(n^2+1\right)^{\frac{1}{2}}\right) \\ &\quad - \left(\frac{2}{\pi}(kb)^3\right)^{\frac{1}{2}} \sin\left(kb + \frac{3\pi}{4}\right) \\ &\quad - \left(\frac{2}{\pi}(nkb)^3\right)^{\frac{1}{2}} \sin\left(nkb + \frac{3\pi}{4}\right). \end{aligned}$$

In (9), k is the wave number, $n = \frac{a}{b}$ is the aspect ratio (greater than or equal to 1), A_n is the membrane surface area, and ρ and c are the density of and speed of sound in the surrounding medium, respectively.

4. Substrate Resistance: $R_{substrate}$: A successful Lamb wave device is efficient in coupling energy from the vibrating mechanism to the substrate. As shown in Fig. 4, the energy sink presented by the substrate can be represented in an equivalent circuit model by the element $R_{\text{substrate}}$. Significant coupling will result when this resistance is much greater than that of other dissipative elements in the circuit. Since the membrane impedance (Z_{mem}) is reactive, the impedance of air (Z_{rad}) is the only other element in this

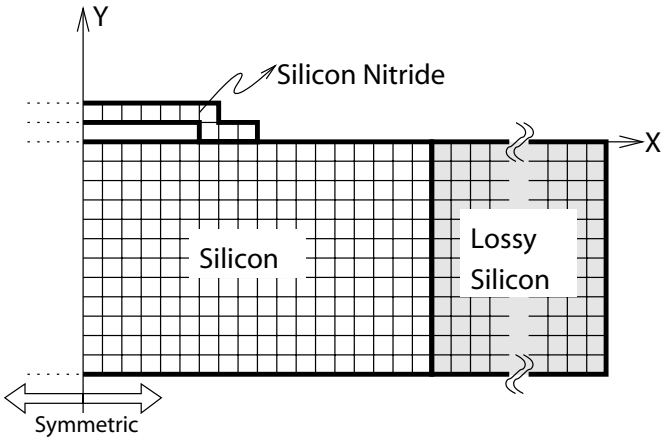

Fig. 7. Finite element mesh of a single membrane.

particular model that has a finite real part. The value of Z_{rad} cannot easily be changed as it is primarily a function of physical constants. Thus, the design goal is to maximize the resistance presented by the silicon substrate.

Note that since the current in the mechanical part of the circuit in Fig. 4 is the membrane velocity, it is important that the definition of $R_{\text{substrate}}$ be consistent with this convention. To that end, if P_n is the average propagating power of the n^{th} Lamb wave mode excited by a membrane with average velocity $\overline{v}$, the expression in (10) can be written for $R_{\text{substrate}}$. The assumption in this formulation is that all of the energy coupled to the substrate is in the form of a propagating mode; for this reason the right-hand side of (10) is purely real.

$$R_{\text{substrate}_n} = \frac{2Pn}{|\overline{v}|^2} \tag{10}$$

Numerical values for the power and the velocity in this equation can be obtained through a two-step process. The first step involves the use of finite element analysis[1] (FEA). FEA is used to determine both the membrane particle velocity v and the stress distribution T across the thickness of the silicon wafer generated by harmonic excitation of the membrane. This is done using a finite element mesh similar to the one depicted in Fig. 7. Since the purpose of the analysis is to characterize wave propagation in the substrate, a lossy section is included at the ends to absorb the incoming energy [32], [43], [44]. The loss coefficient in this region is carefully chosen to minimize the creation of a standing wave pattern due to reflections at the silicon/lossy-silicon interface. This is difficult to do for Lamb wave devices with smaller substrate thicknesses if both the A_0 and S_0 modes are to be detected; the latter mode has a relatively longer wavelength than that of the former, which necessitates a longer lossy region to fully absorb its propagating wave. The short wavelength of the A_0 mode, however, requires a finer mesh to fully capture its behavior. Thus, in order to avoid very long computation times, the fine mesh is used in conjunction with a larger loss coefficient and slightly shorter lossy region to help mitigate reflections of the S_0 mode. It is for this reason that the curve for the 18-μm substrate presented in this section has a slight ripple superimposed on it.

[1]Finite element calculations were performed using Ansys 5.7.

The second step in obtaining numerical values for (10) is to apply normal mode decomposition to the FEA results in an effort to solve for the power in the propagating mode. According to normal mode theory [3], any arbitrary velocity field $\mathbf{v}$(x,y) and associated stress distribution $\mathbf{T}$(x,y) can be expressed as a sum of normal modes:

$$\mathbf{v}(x,y) = \sum_{n=0}^{\infty} a_n(x)\mathbf{v}_n(y) \tag{11}$$

$$\mathbf{T}(x,y) = \sum_{n=0}^{\infty} a_n(x)\mathbf{T}_n(y). \tag{12}$$

In these equations, $a_n(x)$ represents the normal mode amplitudes and $\mathbf{v}_n(x,y)$ and $\mathbf{T}_n(x,y)$ represent the normal velocity and stress distributions, respectively. The normal velocity distributions can be found in [3], and the normal stress fields can be calculated from the equation of motion. The expression for the normal mode amplitude is

$$a_n = -\frac{1}{4P_{nn}} \int_{-h}^{0} \left(v_{x_n}^* T_{xx} + v_{y_n}^* T_{xy} + v_x T_{xx_n}^* + v_y T_{xy_n}^* \right) dy, \tag{13}$$

where v_x, v_y, T_{xx}, and T_{xy} are obtained from FEA. Furthermore, P_{nn} is the average normal mode power per unit length and is given by (14).

$$P_{nn} = -\frac{1}{2}\mathcal{R}\text{e}\left(\int_{-h}^{0} \left(v_{x_n}^* T_{xx_n} + v_{y_n}^* T_{xy_n} \right) dy \right) \tag{14}$$

Using these expressions, the equation of the average propagating power in the wave mode [used in (10)], P_n, can be written

$$P_n = |a_n|^2 P_{nn}. \tag{15}$$

Inherent to the definition presented in (10) for $R_{\text{substrate}}$ is the fact that the vibrating membrane is source of energy of the Lamb wave. This can be verified using FEA/normal mode analysis on the structure illustrated in Fig. 7. The graph in Fig. 8 shows the power coupled into the A_0 mode when forces act on the device electrodes in three different configurations. In the first configuration, in which the forces are on both the top and bottom electrodes, the curve shows a resonant behavior with maximum power delivered to the substrate at the resonant frequency of the membrane. In the second configuration, in which the forces act on the top membrane only, almost the same amount of power is transferred to the substrate at frequencies at and around the membrane resonance. In contrast to these two cases, the energy coupled into the Lamb wave is at least three orders of magnitude smaller when the force is applied to only the bottom electrode. This graph thus clearly

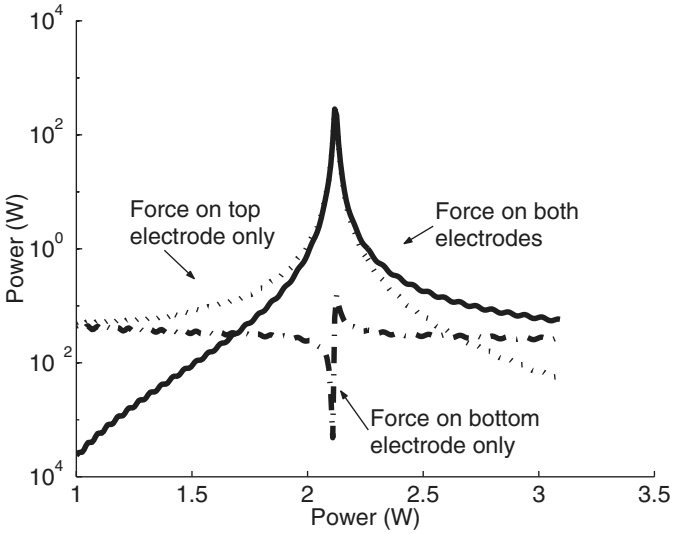

Fig. 8. Power coupled into the A_0 mode of the substrate using three different excitation mechanisms. The constants are taken from (34): $V_s = 5840.9$ m/s, $V_l = 8429.4$ m/s, $\rho = 2332$ kg/m^3. Only the relative value of the different curves is important in this figure. The absolute numbers are a function of the arbitrarily chosen forces applied in the finite element model.

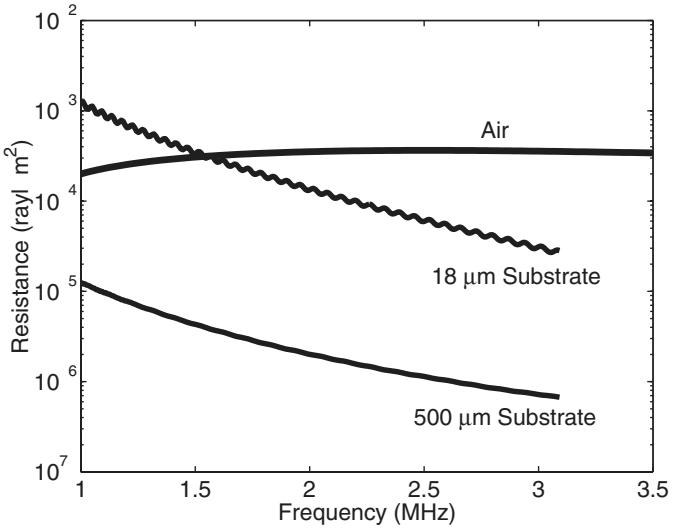

Fig. 9. Resistance presented to the membrane by the A_0 for an 18-μm substrate and a 500-μm substrate. The resistance of air as expressed in (9) is also shown as a point of reference. Constants for silicon are taken from (34): $V_s = 5840.9$ m/s, $V_l = 8429.4$ m/s, $\rho = 2332$ kg/m^3. Constants for air are taken from [45]: $\rho = 1.24$ kg/m^3, $v = 344$ m/s.

shows that the source of most of the energy in the Lamb wave is indeed the vibrating membrane and that the energy is coupled through the supporting posts into the substrate. Note that 95% of the energy coupled into the Lamb wave is in the A_0 mode. For this reason the curves for the S_0 case are not included in Fig. 8.

The graph in Fig. 9 shows the resistance presented to the membrane by the A_0 mode for Lamb wave devices built on both 18- and 500-μm substrates. The 18-μm case is presented because it represents the devices described in this paper. The 500-μm curve is given as a point of comparison as it is the thickness of the first Lamb wave device that was built using CMUTs [30]. For reference, the real part of the air impedance as described by (9) is also shown on the graph. The 18-μm plate presents a resistance that is over two orders of magnitude larger than that of the thicker substrate. Furthermore, the device impedance for the thinner case is now significant relative to the air impedance. This strongly suggests an increase in the amount of energy coupled into the Lamb wave mode and thus better device performance. This finding is consistent with the design of other Lamb wave devices described in the literature that have substrate thicknesses much thinner than the ultrasonic wavelength.

5. Transformer Ratio: n: The transformer ratio n transforms the electrical quantities on the left side of the circuit to mechanical quantities on the right side. Its expression is derived in [42] from the energy constraints of a physically realizable system and assumes that the membrane deflection is identical to that of a piston. The fact that the upper electrode only covers half of the membrane does not affect the value of n because, as shown in [46], the transformer ratio is essentially identical for membranes that are both half and fully metalized. In the equation below, V_{DC} represents the dc bias voltage on the transducer.

$$n = \frac{V_{DC}\epsilon_0\epsilon_r^2 A}{(l_i + l_t + \epsilon_r l_a)^2} \tag{16}$$

6. Parasitic Impedances: C_p, R_{series}, and R_{shunt}: The parasitic capacitance C_p refers primarily to the effects of the traces on the Lamb wave device that lead from the bond pads to the membranes. In the devices described in this paper, C_p is typically 20% of the total CMUT capacitance. R_{series} and R_{shunt} models lead resistances and membrane conductances in the transducer, respectively, that are typically insignificant in the model.

III. Device Fabrication

The process used to fabricate these Lamb wave devices is based on that of the conventional CMUT [40], [47]. Select processing steps are shown in Fig. 10. The base substrate of the device is a (phosphorous) n-type (100) silicon wafer with a resistivity in the 1 to 10 Ω-cm range. The first step in the process is to heavily dope the wafer using a liquid source of phosphorous oxychloride ($POCL_3$) to lower the sheet resistance at the wafer surface to 1.8 Ω/square. This layer acts as the bottom electrode of the capacitor structure. A 2500 Å film of LPCVD low stress silicon nitride (dichlorosilane (DCS) to ammonia (NH_3) ratio of 14:1) is then deposited on the wafer surface; this layer acts as an etch stop for an upcoming potassium hydroxide (KOH) sacrificial etch as well as an insulation layer between the ground plane and the membrane in the completed device.

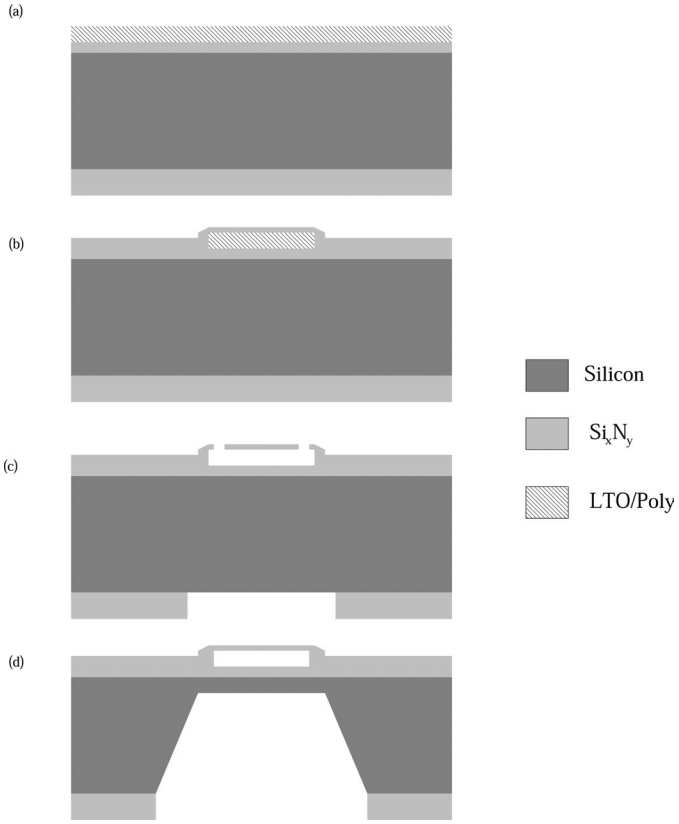

Fig. 10. Select steps of the Capacitive Micromachined Ultrasonic Transducer manufacturing process.

At this point a sacrificial layer of either polysilicon or low-temperature oxide is introduced and patterned to define the shape of the transducer. This is followed by a second layer of LPCVD silicon nitride (DCS:NH_3 ratio of 14:1), which will act as the membrane material. The thickness of both layers is 1 μm. A pattern of etch holes is then created in the top silicon nitride using a reactive ion etching system. This is followed by the etching of the sacrificial layer using either KOH solution or hydroflouric acid.

If KOH is used, most device runs of this nature that are performed in integrated circuit facilities require that wafers go through a decontamination step before going back into mainline equipment. The most common procedure calls for the second half of the RCA clean procedure, also known as SC-2. This cleaning environment is hostile to membranes with large aspect ratios in that it causes them to break; as a result, an alternative was used in the process run of the devices presented in this paper. It should be noted that at this point in the discussion the structure on the wafer is comprised entirely of silicon nitride. This is important because according to [48], the concentration of potassium ions in silicon nitride after an SC-2 clean is 4×10^{11}, while a rinse in deionized water results in only a slightly higher concentration of 5×10^{11}. For reference, a full RCA clean and a piranha clean reduce the potassium ion concentrations to 1×10^{11} and 2×10^{11}, respectively. Both deionized-water and piranha solutions were found to be much less hostile to the device's membranes than were those of the SC-2 procedure.

In order to evacuate and seal the volume underneath the membranes, a third and final silicon nitride layer of the same chemistry as the first two is deposited on the wafer surface. The final two steps in the fabrication of the CMUTs involve a patterned etch on the top surface to create ground pads, and the deposition and patterning of 1500 Å of aluminum (with a 1% concentration of silicon) on the surface to act as the capacitor's top electrode.

Once the fabrication of the transducers is complete, the CMUTs can be characterized to determine their resonant frequency. This frequency, along with the separation of the membranes, is what determines the final substrate thickness of the device. In the specific case of the transducers presented here, the substrate was thinned down to 18 μm. This thinning procedure can be performed using a wet etchant, such as KOH or tetramethyl ammonium hydroxide (TMAH). The former option capitalizes on the perfect masking ability of silicon nitride in KOH [49] and was therefore chosen for use in this process. Due to the high etch rate of aluminum in KOH, a fixture was used to shield the device side of the wafer from the etchant. This fixture, similar to others found in the literature [50], [51] is comprised of two halves of peek that come together over a wafer using a friction o-ring seal. Since the final substrate thickness could not be determined until after the membranes had been built and their resonances had been measured, an etch stop could not be incorporated into the wafer.

It is worth mentioning that many configurations other than that of the fixture were considered for the described thinning procedure. Since the complications were due to the etching of aluminum in KOH, other options included the use of chrome/gold electrodes instead of Al/Si (1%) or of Apiezon (black) wax as a masking material over the electrodes. The former method did not work because the KOH solution destroyed the adhesion between chrome and silicon in areas in which the metal was placed to act as a connection to ground. The latter method failed when high stresses resulting from the applied wax broke the device, while it was thinned in the KOH solution.

IV. Experimental Results and Discussion

The model described by Fig. 4, along with its supporting equations, is verified by experiment as shown in Fig. 11. This figure presents simulated and experimental input impedance plots for fifteen rectangular membranes in parallel with each other. Both the overall shape of the curves and the relative values are similar to what is normally seen in the case of a circular CMUT. Furthermore, the measured resonant frequency and input impedance values agree well with theory, while the bandwidth of the transducer is smaller than predicted by the equivalent circuit. This discrepancy is most likely due to the approximations used in the radiation and device impedance models. Note that in order to satisfy the assumption in the discus-

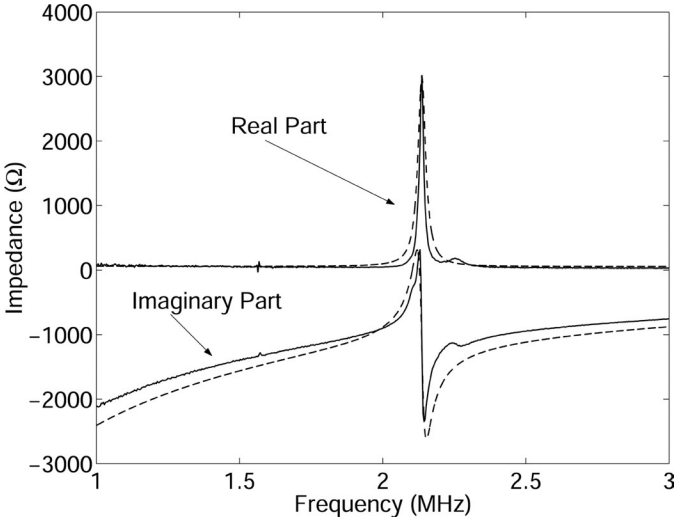

Fig. 11. Experimental (solid line) and simulated (dashed line) input impedance plots of a Lamb wave device with 15 rectangular membranes in parallel with each other on a 350-μm substrate.

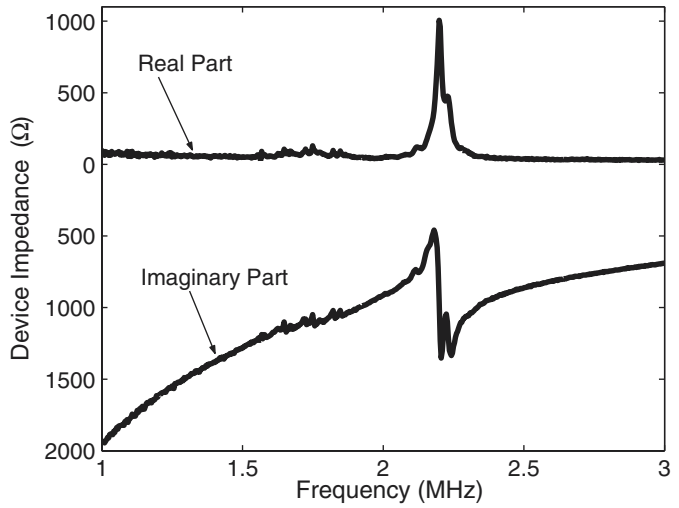

Fig. 12. Measured real and imaginary parts of the input impedance of a Lamb wave device on an 18-μm substrate.

sion of Fig. 4 that $R_{\text{substrate}}$ is small, the transducers used in this measurement have a substrate thickness of 350 μm.

Fig. 12 shows the measured input impedance of the same device used to create the graph of Fig. 11, except that in this case the transducers are on an 18-μm substrate. The plot shows evidence of an increase in the coupling of energy from the membrane to the substrate. Note that at the resonant peak, the input impedance of the thinner device has a larger bandwidth than does its thicker counterpart. These changes are the result of the substrate acting as an energy loss mechanism to the vibrating membrane. From the point of view of the equivalent circuit, the value of $R_{\text{substrate}}$ relative to Z_{rad} has increased with the thinner device substrate. When the value of $R_{\text{substrate}}$ from Fig. 9 is used to predict the input impedance of the device on an 18-μm substrate, the resulting curve does not match very well with experimental data. This is primarily because the thin substrate thickness results in nonuniform stresses on

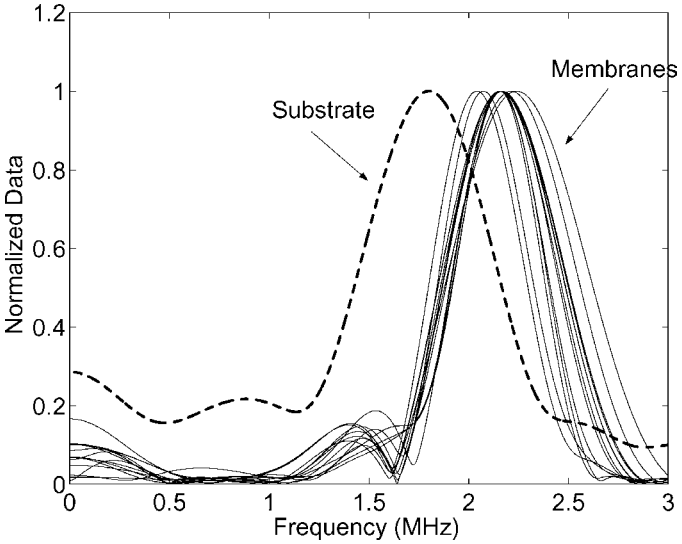

Fig. 13. Normalized impulse response spectra of the membranes (solid lines) and the device substrate (dashed line).

the membrane that affect its impedance in ways that are not yet well understood.

Further evidence of this increased coupling lies in the presence of ripples in the 1.6- to 1.9-MHz range of the graph in Fig. 12. These ripples, which are caused by reflections of the Lamb waves off of the posts of the transducer structures or the edges of the device, are most prominent when the acoustic wavelength is close to the transducer period. From this observation it is clear that there is a mismatch between the frequency of maximum membrane displacement (as defined by its resonance) and the frequency of minimum destructive interference (as defined by the spacing between the CMUT membranes). The solution to this problem is to etch the device substrate to a thickness in which the wavelength of the Lamb wave matches the transducer period. For the devices described here, the ideal thickness is 23 μm. Note that the ripples are not observed in the graph of Fig. 11 because of the minimal coupling of acoustic energy for thick device substrates.

The presence of the frequency mismatch is verified by impulse responses obtained from a laser doppler vibrometer system (PolytecPI Model OFV-3001/OVD-30). Using a laser focused on the membrane surface to measure its displacement, a 3-V, 2.1-MHz electrical pulse was applied to the CMUTs and a fast Fourier transform (FFT) of the resulting waveform was taken to find it spectrum. Note from Fig. 13 that the resonant frequencies of the individual membranes vary from 2.06 to 2.27 MHz, while the substrate displacement spectrum peaks near 1.82 MHz. The former values are a function of the structure's geometry as described by (5). The latter number is determined by the interference between the Lamb waves excited at each membrane as dictated by the transducer period. In order to help show the frequency shifts in a more clear fashion, all of the curves on the graph are normalized with respect to amplitude.

Effects of the mismatch between the membrane resonance and the device geometry also play a strong role in

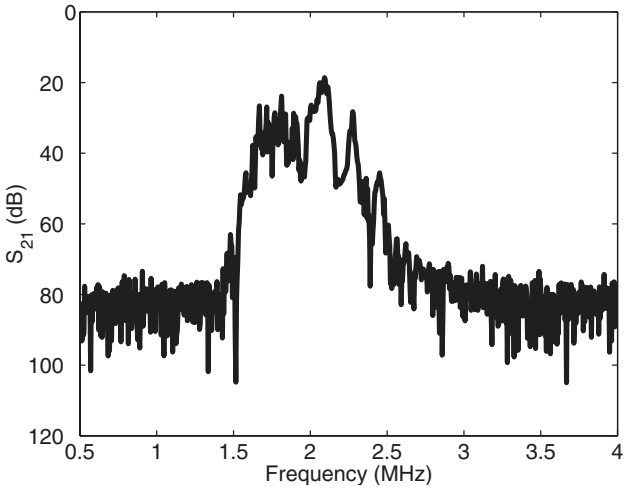

Fig. 14. An S_{21} measurement of a Lamb wave device. Note that the insertion loss near 2.1 MHz is 20 dB.

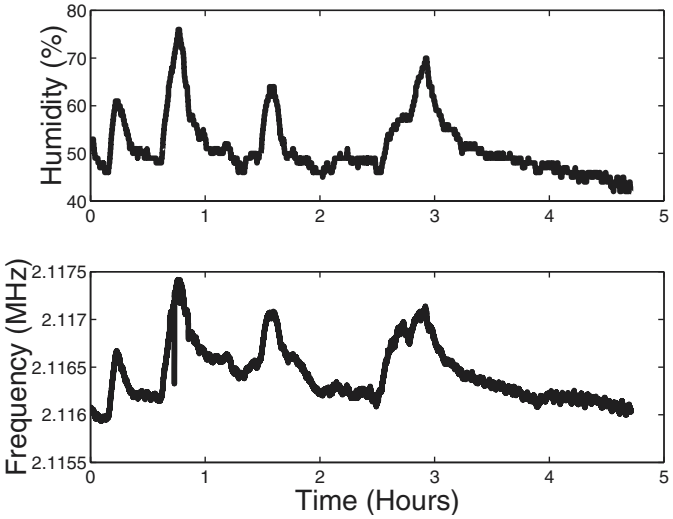

Fig. 15. Humidity measurement at 23°C.

the determination of the insertion loss of the device. As shown in Fig. 14 and confirmed using the delay-line oscillator configuration, at frequencies near the maximum membrane displacement, 2.1 MHz, the insertion loss of the device is 20 dB. This value is attained despite losses created by destructive interference of the Lamb waves in the silicon substrate. The S_{21} plot also shows that the device performs well in the 1.6- to 1.8-MHz range due to the coherent summation of acoustic energy fostered by the membrane locations. The insertion loss at these frequencies is between 25 and 30 dB.

The delay-line setup can also be used to test the ability of the device to work as a sensor. As described above, various loading effects can change the phase velocity of the acoustic wave in the substrate and therefore the frequency of the oscillator. One way to change the loading is to vary the humidity in the environment of the device to cause an absorption of moisture by the material in the channel. Fig. 15 shows the results of an experiment in which the Lamb wave device is put into an environment in which the relative humidity was changing as a function of time, and the temperature was held constant at 23°C. The top graph shows data taken from an off-the-shelf humidity sensor (Omega-RH411), while the bottom graph shows the frequency of the oscillator. The two curves have a similar shape, although the response of the oscillator is slower than that of the humidity sensor. This behavior is expected because the top of the device channel is composed of silicon nitride, which is a hydrophilic material that does not easily desorb moisture. The humidity sensor, on the other hand, is designed to respond quickly to moisture changes in its environment. When evaluating Fig. 15, it is important to remember that the purpose of this experiment was not to show that the Lamb wave device could work as an ideal humidity sensor but rather that it could respond as one would expect to loading.

One additional comment that should be made regarding this experiment is that the CMUT membranes are also affected by changes in the humidity. This phenomenon has little effect on the resulting behavior of the device, however, as the resonant frequency of a vibrating membrane decreases in the presence of mass loading. Since this is the opposite direction of what is measured in Fig. 15, the humidity effects on the channel are dominant in the results presented here.

V. Conclusion

Using rectangular CMUTs, a new type of Lamb wave device has been built. This paper has described these devices, including details of their theory, fabrication, and characterization. The proposed equivalent circuit model and accompanying equations that were presented predict an input impedance that matches well with what is observed by experiment. As indicated using two different measurement techniques, the insertion loss of the transducer is 20 dB despite a mismatch between the resonance of the vibrating membranes and their relative spacing on the 18-μm substrate. The device functions well as a sensor in response to changes of the mass loading of its channel caused by a variation in the humidity in its environment. Future work on these Lamb wave devices includes the fabrication of transducers with a larger substrate resistance and less mismatch between the transducer period and the membrane resonance, as well as a more detailed analysis of the device behavior as a sensor and its response to different measurands.

Appendix A

The derivation of (8) is presented here. It starts with the differential equation governing the normal displacement of a membrane under static conditions:

$$\frac{(Y_0+T)l_t^3}{12(1-\sigma^2)}\nabla^4 u_{DC} - Tl_t\nabla^2 u_{DC} - P + l_t\rho\frac{d^2\omega}{dt^2} = 0. \tag{17}$$

This expression is identical to (4) except for the trivial change of u_{AC} to u_{DC}. Assuming that the aspect ratio is large and using the static nature of the problem to remove the time-dependent term in (17), the membrane response can be reduced to the following one-dimensional problem in the x-direction:

$$\frac{(Y_0+T)l_t^3}{12(1-\sigma^2)}\frac{d^4u_{DC}}{dx^4} - Tl_t\frac{d^2u_{DC}}{dx^2} = P. \tag{18}$$

Using the clamped boundary condition (both the displacement and slope of the displacement of the membrane at the edges is zero) to solve this differential equation under the orientation shown in Fig. 5, the result presented in (8) is obtained (copied below for convenience).

$$u_{DC}(x) = \frac{LP}{8d'k_3'}\left(k_3'L - 4\coth\frac{k_3'L}{2}\right) + \frac{LP}{2d'k_3'}\frac{\cosh k_3'x}{\sinh\frac{k_3'L}{2}} - \frac{Px^2}{2d'} \tag{19}$$

$$k_3' = \sqrt{\frac{d'}{c'}} \quad c' = \frac{(Y_0+T)l_t^3}{12(1-\sigma^2)} \quad d' = Tl_t.$$

Acknowledgments

The authors are grateful to Nancy Latta, Mahnaz Mansourpour, Ulrike Thumser, and Mary Tang at the Stanford Nanofabrication Facility for their help with the fabrication aspects of this project. They would also like to thank Mario Pineda and the rest of the staff at Polytec PI, Inc., for assistance with their Laser Doppler Vibrometer system.

References

[1] H. Lamb, *Proc. Roy. Soc. (London), Ser. A*, vol. 93, 1917, p. 114.
[2] I. A. Viktorov, *Rayleigh and Lamb Waves*. New York: Plenum, 1967, pp. 67–121.
[3] B. A. Auld, *Acoustic Fields and Waves in Solids*. vol. 2, 2nd ed. Malabar, FL: Krieger, 1990, pp. 76–88, pp. 161–162.
[4] K. Toda, "Lamb-wave delay lines with interdigital electrodes," *J. Appl. Phys.*, vol. 44, no. 1, pp. 56–62, 1973.
[5] S. W. Wenzel and R. M. White, "A multisensor employing an ultrasonic Lamb wave oscillator," *IEEE Trans. Electron. Devices*, vol. 35, pp. 735–743, 1988.
[6] S. W. Wenzel, "Applications of Ultrasonic Lamb Waves," Doctoral Dissertation, EECS Department, University of California, Berkeley, CA, 1982.
[7] M. J. Vellekoop, A. J. van Rhijn, G. W. Lubking, and A. Venema, "All-silicon plate wave oscillator system for sensor applications," in *Proc. IEEE Ultrason. Symp.*, 1990, pp. 275–278.
[8] D. F. Fischer, W. J. Varhue, J. Wu, and C. A. Whiting, "Lamb wave microdevices fabricated on monolithic single crystal silicon wafers," *J. Microelectromechanical Syst.*, vol. 9, no. 1, pp. 88–93, 2000.
[9] R. M. White, "Surface elastic waves," *Proc. IEEE*, vol. 58, no. 8, pp. 1238–1276, 1970.
[10] S. W. Wenzel and R. M. White, "Flexural plate-wave sensor: Chemical vapor sensing and electrostrictive excitation," in *Proc. IEEE Ultrason. Symp.*, 1989, pp. 595–598.
[11] R. M. White, "Thermoelastic coupling to Lamb waves," in *Proc. IEEE Ultrason. Symp.*, 1986, pp. 411–415.
[12] R. M. Bozorth, *Ferromagnetism*. Princeton: D. Van Norstrand Co., Inc., 1951, pp. 595–712.
[13] F. L. Degertekin and B. T. Khuri-Yakub, "Single mode Lamb wave excitation in thin plates by hertzian contacts," *Appl. Phys. Lett.*, vol. 69, no. 2, pp. 146–148, 1996.
[14] M. J. Vellekoop, G. W. Lubking, P. M. Sarro, and A. Venema, "Integrated-circuit-compatible design and technology of acoustic-wave-based microsensors," *Sens. Actuators A*, vol. 44, no. 3, pp. 249–263, 1994.
[15] K. Toda and K. Mizutani, "A Lamb wave voltage sensor," *J. Acoust. Soc. Amer.*, vol. 74, no. 3, pp. 677–679, 1983.
[16] R. M. Moroney, R. M. White, and R. T. Howe, "Microtransport induced by ultrasonic Lamb waves," *Appl. Phys. Lett.*, vol. 59, no. 7, pp. 774–776, 1991.
[17] W. Manthey, N. Kroemer, and V. Magori, "Ultrasonic transducers and transducer arrays for applications in air," *Meas. Sci. Technol.*, vol. 3, no. 3, pp. 249–261, 1992.
[18] D. W. Schindel, D. A. Hutchins, L. Zou, and M. Sayer, "The design and characterization of micromachined air-coupled capacitance transducers," *IEEE Trans. Ultrason., Ferroelect., Freq. Contr.*, vol. 42, no. 1, pp. 42–50, 1995.
[19] M. I. Haller and B. T. Khuri-Yakub, "A surface micromachined ultrasonic air transducer," in *Proc. IEEE Ultrason. Symp.*, vol. 2, pp. 1241–1244, 1994.
[20] M. I. Haller and B. T. Khuri-Yakub, "A surface micromachined electrostatic ultrasonic air transducer," *IEEE Trans. Ultrason., Ferroelect., Freq. Contr.*, vol. 43, no. 1, pp. 1–6, 1996.
[21] S. Hansen, N. Irani, F. L. Degertekin, I. Ladabaum, and B. T. Khuri-Yakub, "Defect imaging by micromachined ultrasonic air transducers," in *Proc. IEEE Ultrason. Symp.*, vol. 2, pp. 1003–1006, 1998.
[22] Ö. Oralkan, A. S. Ergun, J. A. Johnson, M. Karaman, U. Demirci, K. Kaviani, T. H. Lee, and B. T. Khuri-Yakub, "Capacitive micromachined ultrasonic transducers: Next generation arrays for acoustic imaging?," *IEEE Trans. Ultrason., Ferroelect., Freq. Contr.*, vol. 49, no. 11, pp. 1596–1610, 2002.
[23] J. McLean and F. L. Degertekin, "Capacitive micromachined ultrasonic transducers with asymmetric membranes for microfluidic applications," in *Proc. IEEE Ultrason. Symp.*, vol. 2, pp. 925–928, 2001.
[24] H. Jagannathan, G. G. Yaralioglu, A. S. Ergun, F. L. Degertekin, and B. T. Khuri-Yakub, "Microfluidic channels with integrated ultrasonic transducers," in *Proc. IEEE Ultrason. Symp.*, vol. 2, pp. 859–862, 2001.
[25] N. Hall and F. L. Degertekin, "An integrated optical detection method for capacitive micromachined ultrasonic transducers," in *Proc. IEEE Ultrason. Symp.*, vol. 1, pp. 951–954, 2000.
[26] S. T. Hansen, A. S. Ergun, and B. T. Khuri-Yakub, "Acoustic sensing using radio frequency detection and capacitive micromachined ultrasonic transducers," in *IEEE MTT-S Intl. Microwave Symp. Digest*, vol. 3, pp. 2243–2246, 2001.
[27] X. C. Jin, F. L. Degertekin, S. Calmes, X. J. Zhang, I. Ladabaum, and B. T. Khuri-Yakub, "Micromachined capacitive transducer arrays for medical ultrasound imaging," in *Proc. IEEE Ultrason. Symp.*, vol. 2, pp. 1877–1880, 1998.
[28] K. Niederer, P.-C. Eccardt, H. Meixner, and R. Lerch, "Micromachined transducer design for minimized generation of surface waves," in *Proc. IEEE Ultrason. Symp.*, vol. 2, pp. 1137–1139, 1999.
[29] Y. Roh and B. T. Khuri-Yakub, "Finite element modeling of capacitor micromachined ultrasonic transducers," in *Proc. IEEE Ultrason. Symp.*, vol. 1, pp. 905–908, 2000.
[30] M. H. Badi, G. G. Yaralioglu, A. S. Ergun, F. L. Degertekin, C. H. Cheng, and B. T. Khuri-Yakub, "A first experimental verification of micromachined capacitive Lamb wave transducers," in *Proc. IEEE Ultrason. Symp.*, vol. 1, pp. 311–314, 2000.
[31] G. G. Yaralioglu, M. H. Badi, A. S. Ergun, C. H. Cheng, F. L. Degertekin, and B. T. Khuri-Yakub, "Lamb wave devices using capacitive micromachined ultrasonic transducers," *Appl. Phys. Lett.*, vol. 78, pp. 111–113, 2001.
[32] G. G. Yaralioglu, F. L. Degertekin, M. H. Badi, B. A. Auld, and B. T. Khuri-Yakub, "Finite element method and normal mode modeling of capacitive micromachined SAW and Lamb wave transducers," in *Proc. IEEE Ultrason. Symp.*, pp. 129–132, 2000.
[33] J. D. Achenbach, *Wave Propagation in Elastic Solids*. Amsterdam: North Holland, 1973, pp. 220–226.
[34] B. A. Auld, *Acoustic Fields and Waves in Solids*. vol. 1, 2nd ed. Malabar, FL: Krieger, 1990, p. 367,378,393.

[35] F. L. Degertekin, J. Pei, B. V. Honein, B. T. Khuri-Yakub, and K. C. Saraswat, "Thin film effects in ultrasonic wafer thermometry," in *Proc. IEEE Ultrason. Symp.*, vol. 3, pp. 1337–1341, 1994.
[36] R. M. White, P. J. Wicher, S. W. Wenzel, and E. T. Zellers, "Plate-mode ultrasonic sensors," *IEEE Trans. Ultrason., Ferroelect., Freq. Contr.*, vol. 34, no. 2, pp. 162–171, 1987.
[37] W. P. Mason, *Electromechanical Transducers and Wave Filters*. New York: D. Van Norstrand Co., Inc., 1942, p. 181.
[38] L. L. Beranek, *Acoustics*. Woodbury: Acoustical Society of America, 1996, pp. 118–122.
[39] A. Caronti, G. Caliano, A. Iula, and M. Pappalardo, "An accurate model for capacitive micromachined ultrasonic transducers," *IEEE Trans. Ultrason., Ferroelect., Freq. Contr.*, vol. 49, no. 2, pp. 159–168, 2002.
[40] X. Jin, "Micromachined Capacitive Ultrasonic Immersion Transducer Array," Doctoral Dissertation, Electrical Engineering Department, Stanford University, Stanford, CA, 2000.
[41] P. R. Stepanishen, "The radiation impedance of a rectangular piston," *J. Sound Vibration*, vol. 55, no. 2, pp. 275–288, 1977.
[42] F. V. Hunt, *Electroacoustics*. College Park, MD: Acoustical Society of America, 1982, pp. 180–181.
[43] E. Moulin, J. Assaad, C. Delebarre, and D. Osmont, "Modeling of Lamb waves generated by integrated transducers in composite plates using coupled finite element-normal modes expansion method," *J. Acoust. Soc. Amer.*, vol. 107, no. 1, pp. 87–94, 2000.
[44] A. Bozkurt, F. L. Degertekin, A. Atalar, and B. T. Khuri-Yakub, "Analytic modeling of loss and cross-coupling in capacitive micromachined ultrasonic transducers," in *Proc. IEEE Ultrason. Symp.*, vol. 2, pp. 1025–1028, 1998.
[45] G. Kino, *Acoustic Waves*. Princeton: Prentice Hall, Inc., 1987, p. 553.
[46] A. Bozkurt, I. Ladabaum, A. Atalar, and B. T. Khuri-Yakub, "Theory and analysis of electrode size optimization for capacitive microfabricated ultrasonic transducers," *IEEE Trans. Ultrason., Ferroelect., Freq. Contr.*, vol. 46, no. 6, pp. 1364–1374, 1999.
[47] V. Foglietti, D. Memmi, G. Caliano, E. Cianci, F. Galanello, and M. Pappalardo, "Fabrication of micromechanical capacitive ultrasonic transducers by surface micromachining," in *Proc. Internat. Conf. Microtechnologies*, vol. 1, pp. 79–82, 2000.
[48] M. Aslam, B. E. Artz, S. L. Kaberline, and T. J. Prater, "A comparison of cleaning procedures for removing potassium from wafers exposed to KOH," *IEEE Trans. Electron. Devices*, vol. 40, no. 2, pp. 292–295, 1993.
[49] H. Seidel, L. Csepregi, A. Heuberger, and H. Baumgärtel, "Anisotropic etching of crystalline silicon in alkaline solutions," *J. Electrochem. Soc.*, vol. 13, no. 11, pp. 3612–3625, 1990.
[50] C.-H. Han and E. S. Kim, "Fabrication of dome-shaped diaphragm with circular clamped boundary on silicon substrate," in *12th Intl. Workshop on Micro Electro Mechanical Systems*, 1999, pp. 505–510.
[51] G. C. Hilton, J. M. Martinis, K. D. Irwin, N. F. Bergren, D. A. Wollman, M. E. Huber, S. Deiker, and S. W. Nam, "Microfabricated transition-edge x-ray detectors," *IEEE Transactions on Applied Superconductivity*, vol. 11, no. 1, pt. 1, pp. 739–742, 2001.

Mohammed H. Badi (S'00) was born in Toronto, Canada. He earned his B.A. in French and B.S. in electrical engineering in 1997 and his M.S. in electrical engineering in 1999, all from Stanford University. He is currently at Stanford pursuing a doctoral degree in electrical engineering.

His research interests include micromachined sensors and actuators, analog/RF circuit design, and semiconductor device physics. His current research focuses on Lamb wave and SAW devices using Capacitive Micromachined Ultrasonic Transducers (CMUTs). He was a recipient of the National Honor Society Scholarship and is a member of the Tau Beta Pi honor society.

Goksen G. Yaralioglu (S'92–M'99) was born in Akhisar, Turkey, in 1970. He received his B.S. and Ph.D. degrees from Bilkent University in 1992 and 1997, respectively, both in Electrical and Electronics Engineering. His thesis work was on atomic force microscopy. He is currently an Engineering Research Associate at Stanford University. His recent research interests include design and application of micromachined ultrasonic transducers, smart microfluidic channels with integrated ultrasonic transducers and characterization using atomic force microscope at ultrasonic frequencies.

A. Sanli Ergun (S'91–M'99) was born in Ankara, Turkey, in 1969. He received his B.Sc., M.Sc., and Ph.D. in 1991, 1994, and 1999, respectively, all in Electrical and Electronics Engineering from Bilkent University, Turkey. He is now in the E. L. Ginzton Laboratory, Stanford University as an engineering research associate. His research interests are microwave electronics, ultrasonics, MEMS, and specifically CMUTs.

Sean T. Hansen (S'00) graduated with his B.S. and M.S. degrees in electrical engineering from Stanford University in 1997 and 1999. He is currently a doctoral candidate in electrical engineering at the E. L. Ginzton Laboratory at Stanford University. His research interests include capacitive micromachined ultrasonic transducers, microphones, and radio frequency electronics. He is a member of the IEEE and the Tau Beta Pi engineering honor society.

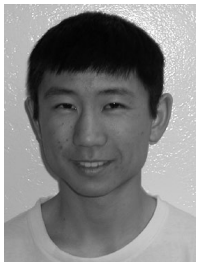

Eehern J. Wong was born in Sacramento, CA. He received a B.S. degree with distinction in 2002 and is currently pursuing an M.S. degree, also in electrical engineering, at Stanford University. From the summer of 2000 through June 2001, he interned as a process engineer for the Khuri-Yakub Group in the E. L. Ginzton Laboratory. His work there included research in thin nitride films and the creation of microstructures to determine their stresses. He focused his undergraduate course work in control theory and is currently following this interest in controls and analog electronics. He currently works in the Aero/Astro department under Professor Lall, creating autonomous robots for cooperative networked control of dynamical peer-to-peer vehicle systems. He is a member of Tau Beta Pi.

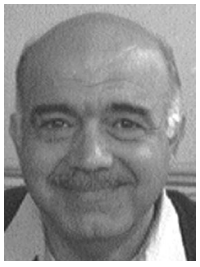

Butrus T. Khuri-Yakub (S'70–S'73–M'76–SM'87–F'95) was born in Beirut, Lebanon. He received the B.S. degree in 1970 from the American University of Beirut, the M.S. degree in 1972 from Dartmouth College, and the Ph.D. degree in 1975 from Stanford University, all in electrical engineering. He joined the research staff at the E. L. Ginzton Laboratory of Stanford University in 1976 as a Research Associate. He was promoted to Senior Research Associate in 1978 and to Professor of Electrical Engineering (Research) in 1982.

He has served on many university committees in the School of Engineering and the Department of Electrical Engineering.

Presently, he is the Deputy Director of the E. L. Ginzton Laboratory. Professor Khuri-Yakub has been teaching both at the graduate and undergraduate levels for more than 15 years, and his current research interests include *in situ* acoustic sensors (temperature, film thickness, resist cure, etc.) for monitoring and control of integrated circuits manufacturing processes, micromachining silicon to make acoustic materials and devices, such as airborne and water immersion ultrasonic transducers and arrays, and fluid ejectors, and in the field of ultrasonic nondestructive evaluation and acoustic imaging and microscopy.

Professor Khuri-Yakub is a fellow of the IEEE, a senior member of the Acoustical Society of America, and a member of Tau Beta Pi. He is associate editor of *Research in Nondestructive Evaluation*, a journal of the American Society for Nondestructive Testing. He has authored more than 300 publications and has been principal inventor or coinventor of 52 issued patents. He received the Stanford University School of Engineering Distinguished Advisor Award, June 1987, and the Medal of the City of Bordeaux for contributions to NDE, 1983.